Influence of the Interfacial Phase on the Structural Integrity and Oxygen Permeability of a Dual-Phase Membrane

Ming Sun,[†] Xinwei Chen,[†] and Liang Hong*,[†,‡]

[†]Department of Chemical and Biomolecular Engineering, National University of Singapore, BLK E5 02-02, 4 Engineering Drive 4, Singapore 117576, Singapore

[‡]Institute of Materials Research and Engineering, 3 Research Link, Singapore 117602, Singapore

ABSTRACT: Compositing fluorite $Ce_{0.8}Gd_{0.2}O_{2-\delta}$ (CGO) oxide with perovskite $La_{0.4}Ba_{0.6}Fe_{0.8}Zn_{0.2}O_{3-\delta}$ (LBFZ) oxide leads to the formation of a minor interfacial $BaCeO_3$ phase upon sintering at 1400 °C. This interfacial composition assures a gastight ceramic membrane with fine grain-boundary structure, in which the LBFZ phase exhibits an improved oxygen permeability over the pristine LBFZ membrane on the same volumetric basis. The presence of the $BaCeO_3$ phase effectively preserves the structural integrity of the composition by limiting the interfacial diffusion of barium ions between LBFZ and CGO. In comparison, replacing CGO with $Y_{0.08}Zr_{0.92}O_{2-\delta}$ in the system results in a substantially low oxygen flux due to an overwhelming interfacial diffusion and, consequently, a heavy degradation of LBFZ. Besides structural reinforcement, the high interface between LBFZ and CGO benefits oxygen transport, as is proven through variation of the oxygen partial pressure on the feed side of the membrane and operation temperature. Furthermore, the trade-off between LBFZ loading and interfacial diffusion yields an optimal CGO loading at 40 wt %, which exhibits an oxygen flux of 0.84 $cm^3/cm^2\cdot min$ at 950 °C. In summary, the minor interfacial binding between CGO and LBFZ grains is constructive in easing oxygen crossover in the phase boundary with the exception of maintaining membrane structural stability under oxygen permeation conditions.

KEYWORDS: perovskite−fluorite composite, oxygen permeation, interfacial diffusion, air separation, tubular membrane
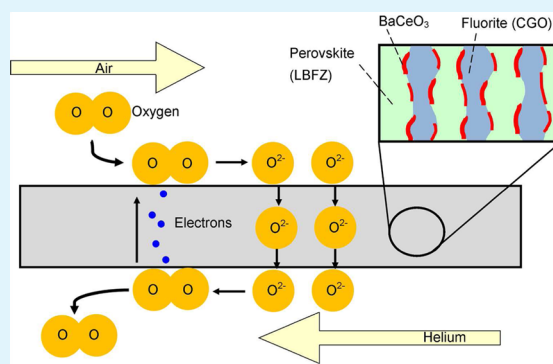
1. INTRODUCTION

Mixed ionic electronic conductor (MIEC) materials have been used to fabricate a specific membrane to separate oxygen from air through an electrochemical redox mechanism at high temperatures (750−950 °C)[1−3] and to form a cathode of solid oxide fuel cells[4,5] and gas sensors.[6,7] A complete dense MIEC membrane promises infinite permselectivity for oxygen because only lattice oxygen ions (O^{2-}) could transport through the membrane. This distinct value has prompted paramount explorations of various perovskite-type MIEC membranes[8−15] over the last 3 decades. However, a list of stringent requirements is needed to be fulfilled before any possible industrial application. This includes achieving a gastight matrix in a sufficiently thin membrane, maintaining its perovskite structure under reducing atmosphere (e.g., methane and syngas) when partial methane reforming (POM) is incorporated to drive oxygen permeation on the permeate side,[15,16] and enduring lattice stress caused by an increase in the concentration gradient of oxygen vacancy between the two phases of the membrane and the phase transition from a rhombohedral to a cubic crystal system during operation.[17−19] In short, both the chemical and mechanical stability criteria remain a huge challenge to a practical useful MIEC membrane.

Recent progress in evolving cobalt-free perovskite has successfully enhanced the chemical stability of the MIEC membrane, whose permeate facet is exposed to the corrosive reaction atmosphere of POM.[20,21] With respect to the lattice stress originating from the structural expansion mismatch, incorporating a precious metal into the bulk phase of a ceramic oxygen electrolyte membrane demonstrated a possible route to effectively tackle the stability issue.[22] The effect is attributed to the enhancing role of the noble metal phase in the exchange rate of oxygen at the surface of the membrane,[22] thus minimizing the possibility of crack formation. However, the high cost of noble metal and thermal expansion mismatch between the two phases is the primary concern of this composite system.

When a similar rationale is applied, the ceramic−ceramic composite membrane matrix consisting of a fluorite-type oxygen electrolyte and a perovskite MIEC presents an alternative promising option. Kharton et al.[23−25] investigated this type of dual-phase composite that comprises $Ce_{0.8}Gd_{0.2}O_{2-\delta}$ (CGO) and $La_{0.7}Sr_{0.3}MnO_{3-\delta}$ (LSM), while Zhu and Yang[15] reported a composite membrane that comprises of 60 wt % CGO and 40 wt % $Gd_{0.2}Sr_{0.8}FeO_{3-\delta}$, both of which achieved initial success in overcoming structural

vulnerability. Nevertheless, a dual-phase composite system requires careful attention on the compatibility issue and maintenance of the structural integrity of both phases at high temperature. In particular, compatibility between the two phases is essential to ensuring that there is no occurrence of interstice along the boundary between them during sintering. Moreover, sintering between the two phases often incurs interfacial diffusion due to ionic transfer from perovskite (e.g., LSM) to fluorite (e.g., CGO), resulting in an interfacial barrier. As such, the extensive growth of such a barrier is detrimental to oxygen transport between two phases.

This problem can be circumvented by realizing a trade-off between the ionic conduction and structural stability rather than by relying on a stable perovskite. Two recent works reflect the progress of this endeavor: (1) The disk membrane comprising perovskite $Sm_{0.6}Sr_{0.4}FeO_3$ and fluorite oxide $Ce_{0.85}Sm_{0.15}O_{1.925}$ demonstrated a maximum oxygen flux of 0.8 $cm^3/cm^2\cdot min$ at 940 °C and log $P_{O_2}'/P_{O_2}'' = 1.65$, which was maintained by helium purging on the permeate side.[26] (2) The $Pr_{0.6}Sr_{0.4}FeO_{3-\delta}/Ce_{0.9}Pr_{0.1}O_{2-\delta}$ composite membrane showed a maximum oxygen flux of 4.4 $cm^3/cm^2\cdot min$ with the use of dry reforming of methane at 950 °C on the permeate side to maintain the oxygen gradient.[27]

This work commences with a finding that impacts the stability and structural integrity of a perovskite–fluorite dual-phase membrane. We selected the perovskite $La_{0.4}Ba_{0.6}Fe_{0.8}Zn_{0.2}O_{3-\delta}$ (LBFZ) to combine with fluorite CGO because LBFZ possesses high O^{2-}/e^- conductivity and excellent chemical stability against reduction in the methane-dry-reforming atmosphere.[28] The phenomenon centers around the limited interfacial diffusion of barium ion (Ba^{2+}) between LBFZ and CGO, which results in $BaCeO_3$ microdomains on the surface of the CGO grains. Upon generation, this minor interfacial phase blocks further diffusion of Ba^{2+} ions, which satisfies the need for a thin interfacial diffusion layer consisting of dispersion of microdomains. The existence of such a particular interfacial layer would be favorable because it bonds the two phases and would not impede oxygen transport across the phase boundary, as depicted in the photograph in the Abstract. In contrast to the LBFZ–CGO combination, replacement of CGO by $Y_{0.08}Zr_{0.92}O_{2-\delta}$ (YSZ) induces a significant interfacial diffusion of Ba^{2+} ions from LBFZ to YSZ and, consequently, undermines the oxygen permeability through the composite membrane. Such a result reflects the importance of a diffusion barrier in maintaining the stability of the membrane. Therefore, this research focuses on the CGO–LBFZ composite membrane by examining the effect of the phase composition of the membrane on the oxygen flux, where an optimal loading of LBFZ was identified based on the maximum oxygen permeation flux. In addition, the role of CGO in the dual-phase composite was investigated by temperature-dependent profiles of hydrogen reducibility and oxygen desorbability with variation of the LBFZ loading, conducted at different temperatures or by setting different oxygen partial pressure drops across the membrane.

2. EXPERIMENTAL SECTION

2.1. Materials Used. Lanthanum(III) nitrate hexahydrate [La-$(NO_3)_3\cdot 6H_2O$; ≥99%, Fluka], zinc(II) nitrate hexahydrate [Zn-$(NO_3)_2\cdot 6H_2O$; ≥99%, Fluka], iron(III) nitrate nonahydrate [Fe-$(NO_3)_3\cdot 9H_2O$; ≥98%, Sigma Aldrich], and barium nitrate [Ba($NO_3)_2$; ≥98%, Sigma Aldrich] were used without further purification. Other chemicals used in the preparation of the oxide powders included an ammonium solution (25%, Merck), ethylenediaminetetraacetate (EDTA; ACS reagent, 99.4%, Sigma Aldrich), and poly(vinyl alcohol) (80% hydrolyzed; M_w = 9000−10000; Sigma Aldrich). Yttria (8 mol %)-stabilized zirconia (YSZ; median diameter = 0.5−1.0 μm; specific surface area > 15 m^2/g) was purchased from Stanford Materials. Analytical-grade toluene (Fisher Scientific) and methyl ethyl ketone (MEK; Sigma Aldrich) were used to dissolve the binder, poly(vinyl butyral) (Butiva-79; Monsanto). Ceramic sealant (AL/CS Binder and Filler, Minco UK Ltd.) and silver paint (SPI Supplies Division of Structure Probe, Inc.) were used to seal the ends of the ceramic membrane for oxygen permeation examination.

2.2. Preparation of Ceramic Powders and a Tubular Membrane Reactor. The LBFZ and CGO powders were prepared by the modified Pechini method.[29] Stoichiometric amounts of La($NO_3)_3\cdot 6H_2O$, Ba($NO_3)_2$, Fe($NO_3)_3\cdot 9H_2O$, Zn($NO_3)_2\cdot 6H_2O$, and EDTA with the designated molar ratio of 2:3:4:1:10 were added in deionized water to formulate a suspension of about 0.8 M of the total solutes. The suspension became a clear solution after ammonia was added to it to a value of pH 8−9 because of dissolution of $EDTA^{4-}(NH_4^+)_4$. Intermediate chelation of the $EDTA^{4-}$ anion with the metal ions formed a deep-brown solution. After that, a small amount of poly(vinyl alcohol) (5 wt % of EDTA) was then added as a thickener in the solution to form the precursor solution. Subsequently, the solution was heated to 80−100 °C and thickened until a metalloorganic gel was formed. Similarly, a solution composed of Ce($NO_3)_3\cdot 6H_2O$, Gd($NO_3)_3\cdot 6H_2O$, citric acid, and glycine in deionized water by a molar ratio of 4:1:5:5 was formulated and eventually converted to gel. The two gels were then pyrolyzed at 400 °C for 2 h and then calcined at 1000 and 1200 °C, respectively, each for 2 h in air. Both the heating and cooling rates were fixed at 3 °C/min. Fine powders of LBFZ and CGO were ultimately obtained.

To fabricate a tubular membrane, a slurry with 32 wt % solid loading was prepared by mixing LBFZ powder with either CGO powder or YSZ powder in a predetermined ratio in a liquid solution consisting of toluene/MEK (1:1, v/v) and Butiva-79 (2 wt % of the mixture). The slurry was ball-milled with zirconia balls for 1 day to ensure substantial mixing of the powders. After evaporation of the solvent, the dried solid left was ground and sieved through a 45-μm mesh. The powder was filled into a tubular mold with a mandrel and pressed to 35000 psi in a cold isostatic press (Avure Technologies Inc.) to prepare a green tube (7.0 mm o.d. × 4.7 mm i.d. × 200 mm length). This green tube was then subjected to a sintering profile in air as such: (1) heating at a rate of 2 °C/min to 400 °C and dwelled for 1 h, (2) heating at a rate of 2 °C/min to 1400 °C and dwelled for 4 h to allow densification of the membrane matrix. A sintered tubular membrane with a tube wall of 0.9−1.0 mm thickness and 6 mm diameter was prepared. For sample identification purposes, the membrane denoted by CGO−LBFZ40 signifies that it comprises 60 wt % CGO powder and 40 wt % LBFZ. In addition, a tubular membrane made of pure LBFZ was prepared as a control sample.

2.3. Instrumental Characterization. The powder sample of a CGO−LBFZ composite required for carrying out the following characterizations except scanning electron microscopy (SEM; JEOL JSM-6700F) was prepared by smashing a small piece of the sintered composite tubular membrane and then thoroughly grinding the chunks until a very fine powder was obtained. Powder X-ray diffraction (XRD) was performed on a diffractometer (Shimadzu XRD-6000, Cu Kα radiation) using a scanning rate of 3°/min and a step width of 0.02° in the range from 20 to 80°. The microstructures of the surface and bulk of the membrane were scrutinized on a SEM. To check the interfacial phase observed from XRD, a small amount of fine powder was dispersed in ethanol by intense sonication for a few minutes. The top suspension layer was then extracted and dripped onto a copper grid to deposit sparse particles on the grid. The sample was examined on a transmission electron microscope (TEM; JEOL 2000FXII). The oxygen temperature-programmed desorption (O_2-TPD) and temperature-programmed reduction (TPR) properties of a composite oxide powder were analyzed on an Autosorb-1 instrument (Quantachrome Instruments). For O_2-TPD analysis, 500 mg of the sample was loaded and scanned from 50 to 950 °C using a heating rate of 10 °C/min

under a helium gas purge (80 mL/min). For TPR, each test used 60 mg of the sample and the temperature scan was conducted in 5% H_2/N_2. The XRD patterns of the samples after the TPR scan were also examined, and the samples are labeled by the suffix "R".

2.4. Oxygen Permeation Test. The oxygen permeability through a tubular composite membrane was measured using the setup illustrated in Figure 1. The central part of the tubular membrane (2
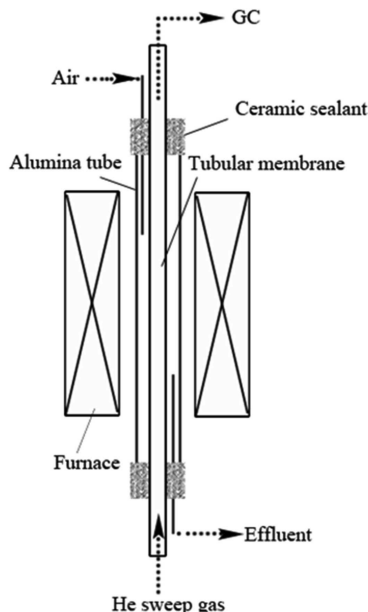

Figure 1. Design of the reactor setup to house the tubular membrane to investigate oxygen separation from air at high temperature.

cm length) was used to perform oxygen permeation, and the rest of the surface was first coated with silver paint and subsequently covered by a ceramic sealant to ensure no leakage. After drying, the two ends of the membrane were bound with two alumina extension tubes with a slightly smaller diameter using the ceramic sealant. After that, the tube was fixed in a larger alumina tube to complete the setup. The setup was then vertically placed in the heating zone of a tube furnace. The external surface of the membrane was selected as the purging side, over which an air stream (200 cm^3/min) was maintained, and the inner side as the permeate side, where a sweep gas flow (helium, 40 cm^3/min) was maintained. The sweep stream from the permeate side was injected into a gas chromatograph (PerkinElmer ARNEL, Clarus 500) to determine the concentration of oxygen. The oxygen permeation flux (J_{O_2}, cm^3/cm^2·min) was therefore calculated by eq 1:[30]

$$ J_{O_2} = \left(C_{O_2} - \frac{21}{79} \sqrt{\frac{28}{32} C_{N_2}} \right) \frac{F}{S} \tag{1} $$

in which C_{O_2} and C_{N_2} are the exit concentrations (%) of oxygen and nitrogen in the sweep stream, respectively, F (cm^3/min) is the flow rate of the sweep gas, and S (cm^2) is the permeation surface area.

Defined by eq 2, leakages of less than 5% were detected in all of the oxygen permeation tests, which is due to imperfect sealing at the two joint junctions. Because each measurement of the oxygen flux was carried out after the separation reached steady state, the readings underwent negligible fluctuation with time.

$$ \text{leakage} = \frac{21}{79} \sqrt{\frac{28}{32}} \frac{C_{N_2}}{C_{O_2}} \times 100\% \tag{2} $$

3. RESULTS AND DISCUSSION

3.1. Interfacial Characteristics of the Two Dual-Phase Composites. Integration of a fluorite oxide, i.e., CGO or YSZ, with the perovskite LBFZ oxide to form a dual continuous phase membrane aims to preserve the structural integrity and maintain the mixed conductivity of the LBFZ phase at the temperatures of oxygen transport. In addition to the structural strengthening role, the fluorite phase serves as an additional O^{2-}-transfer channel. For an ideal situation, both phases must remain intact at high temperatures during sintering and gas separation operation. However, the tendency of interfacial mass diffusion at high temperatures cannot be ignored and has to be curbed to ensure the structural integrity of the membrane.

As observed in Figure 2, both CGO−LBFZ40 and YSZ−LBFZ40 composites display very different degrees of interfacial reactivity by a comparison of their respective XRD patterns. In the case of CGO−LBFZ40, although the composite still retained the dual-phase structure, minor impurity diffraction peaks ($2\theta = 28.72°$, $41.14°$, and $50.88°$), which are identified to be the interfacial phase of either $BaCeO_3$ (JCPDS 82-2425) or $Ba(Ce_{0.9}Gd_{0.1})O_{2.95}$ (JCPDS 81-1385; Figure 2a), are present. This can be attributed to the interfacial diffusion of Ba^{2+} from LBFZ to CGO at the sintering temperature. Transmission electron microscopy (TEM) examination also exhibits a narrow strip between the two phases in this composite (Figure 3), which could be assigned as the diffusion layer because it presents a lattice pattern different from that of the two main phases. A similar characterization was also quoted in the article.[26] Rationally, this interfacial phase must have prevented
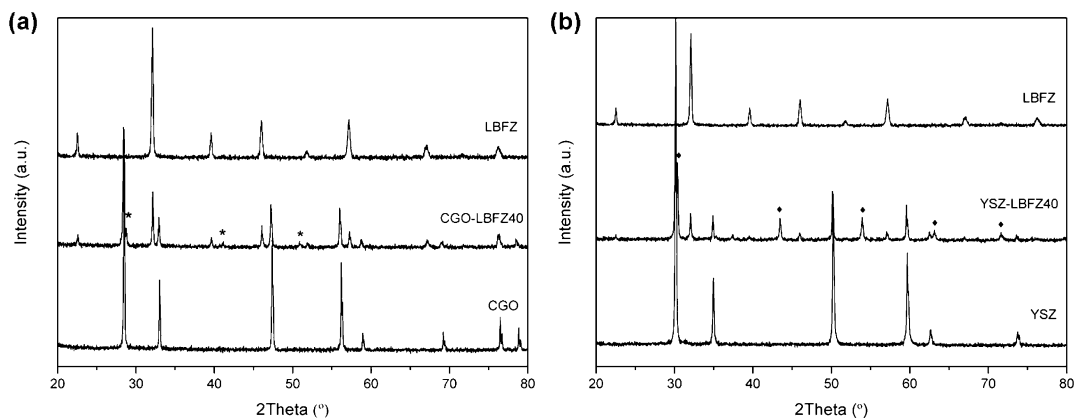

Figure 2. XRD patterns of (a) LBFZ, CGO, and CGO−LBFZ40, (*) $Ba(CeO_3)$ or $Ba(Ce_{0.9}Gd_{0.1})O_{2.95}$, (b) LBFZ, YSZ, and YSZ−LBFZ40, (♦) $BaZrO_3$.

9069

dx.doi.org/10.1021/am4023384 | ACS Appl. Mater. Interfaces 2013, 5, 9067−9074
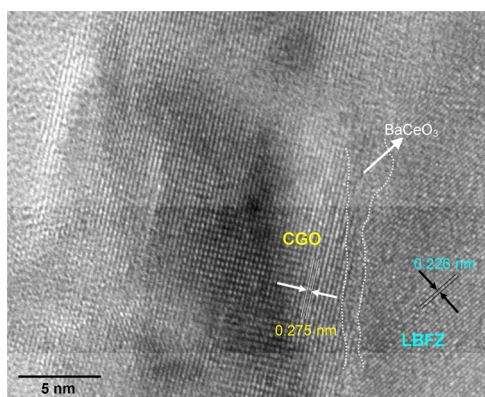
Figure 3. TEM micrographs of CGO−LBFZ40, showing the distinct phases of CGO (fluorite phase) and LBFZ (perovskite phase) with a small extent of the interfacial phase of BaCeO₃.

further diffusion of Ba^{2+} and, hence, limits it to a trivial extent. On the contrary, a far more significant interfacial reaction took place in the YSZ−LBFZ40 composite, as is proven by the emergence of a set of new peaks at (2θ = 30.36°, 43.44°, 53.94° 63.16°, and 71.66°), which are the fingerprint of BaZrO₃ (JCPDS 74-1299) in Figure 2b. Accompanying this heavy extent of the interfacial reaction, the LBFZ perovskite structure degraded almost completely because of the departure of Ba^{2+} ions from it. In comparison, the fluorite YSZ structure remains unaltered during the course of sintering. This investigation indicates that CGO is an appropriate oxide electrolyte to combine with LBFZ.

According to TPR characterization, a comparison of the CGO−LBFZ40 curve with the pristine LFBZ curve reflects the change in the reducibility of LBFZ due to significant interfacing with CGO (Figure 4). The TPR profile of pristine LBFZ shows
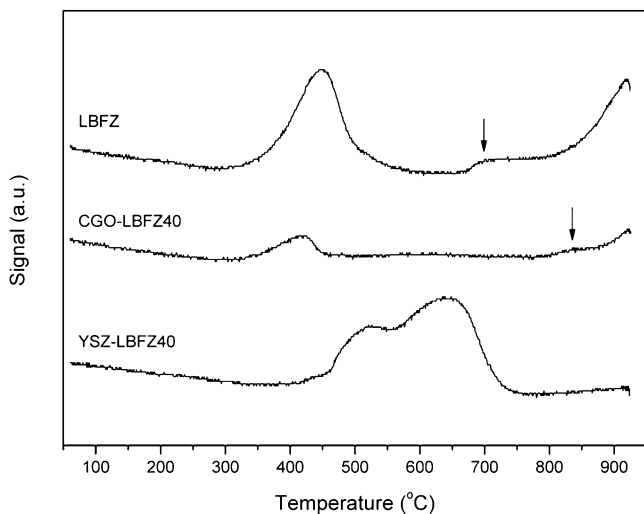

Figure 4. TPR profiles of LBFZ, CGO−LBFZ40, and YSZ−LBFZ40.

three peaks at ca. 448, 705, and 919 °C, which reflects the different reduction steps of iron ions from the highest oxidation state of 4+ to iron metal, as observed in our previous work in which the LBFZ perovskite structure was sintered at 1200 °C.[28] It is noted that in the present work LBFZ was sintered at 1400 °C and, hence, the first TPR reduction step is deferred by 50 °C because of its reduced surface reactivity. Relative to the pristine LBFZ, the LBFZ phase in the CGO−LBFZ40

composite shows a significantly smaller peak area than it should have by loading and a slight decrease in the first reduction peak temperature under the same analysis condition. Moreover, its second reduction peak (labeled by an arrow) emerges at a higher temperature and is much weaker than that of the pristine LBFZ.

This comparison shows the stabilizing effect of the CGO phase. From the SEM micrographs, it can be seen that the CGO−LBFZ40 composite (Figure 5a) contains apparently smaller LBFZ grain sizes in cubiclike shape than those found in the pristine LBFZ (Figure 5c). This was evident upon close inspection of the XRD pattern in Figure 2a. When the LBFZ peaks of CGO−LBFZ40 were compared with those of the pristine LBFZ, it was found that those in the composite were distinctly narrower. This shows that a greater size of the perovskite crystallites was achieved in the course where the CGO−LBFZ40 composite was sintered. Moreover, it can be proposed that the CGO phase plays a role in inducing "recrystallization" of LBFZ through formation of the interfacial phase during sintering. From the perspective of surface thermodynamics, there must be a surface stabilization mechanism to stabilize the smaller LBFZ grains. It is proposed that the partitioning role of CGO is critical to confining the aggregation trend of the LBFZ grains during sintering. In addition, when the smooth surface morphology of the pristine LBFZ (Figure 5c) is compared, both the LBFZ cubic particles and CGO lumps in the composite (Figure 5a) show a rough surface. It is presumed that CGO undergoes a very slight sublimation because its vapor pressure is 10 Pa at 1300 °C, which causes thin deposition on the LBFZ phase, as shown by tiny blisters, and, consequently, protects LBFZ from being effectively reduced by hydrogen, as justified by its TPR. As far as the TPR profile of YSZ−LBFZ40 is concerned, two strong overlapped peaks emerge at about 525 and 650 °C. This outcome is consistent with the XRD of the composite; that is, the reducibility of iron ions is largely promoted because of degradation of the LBFZ phase. Hence, as observed in Figure 5d, YSZ−LBFZ40 exhibits two types of grains that are different in size; the big one is presumed to be YSZ doped by Ba^{2+}, while the small one is the degraded LBFZ by virtue of their loadings by weight. The image also shows prevailing sintering of the Ba-YSZ phase, which disrupts connection of the degraded LBFZ phase.

3.2. Impact of the Composite Membrane Structure on Oxygen Permeation. Three tubular ceramic membranes (∼1 mm tube wall) made of LBFZ and the above two dual-phase composites were used to conduct air separation to examine their oxygen permeability, which is driven by helium sweeping on the permeate side. The testing outcome showed a linear temperature dependence (Figure 6), which reflects the existence of a steady concentration of lattice oxygen vacancies in each membrane. The LBFZ membrane displayed the highest oxygen permeation flux among the three as expected, e.g., attaining a flux as high as 0.835 cm³/cm²·min at 950 °C ($10^4/T$ = 8.1 K^{-1}). The composite membrane CGO−LBFZ40 manifested 55% flux of the pristine LBFZ membrane at 950 °C. This percentage is in effect greater than the LBFZ loading in the composite and thus implies that the CGO phase does contribute to the oxygen flux. Because oxygen enters the membrane (via a cathodic reaction) from air flow and leaves the membrane (via an anodic reaction) to helium purge only at the LBFZ sites on the respective surfaces, there must be an O^{2-} stream crossing over the interfacial boundary between CGO
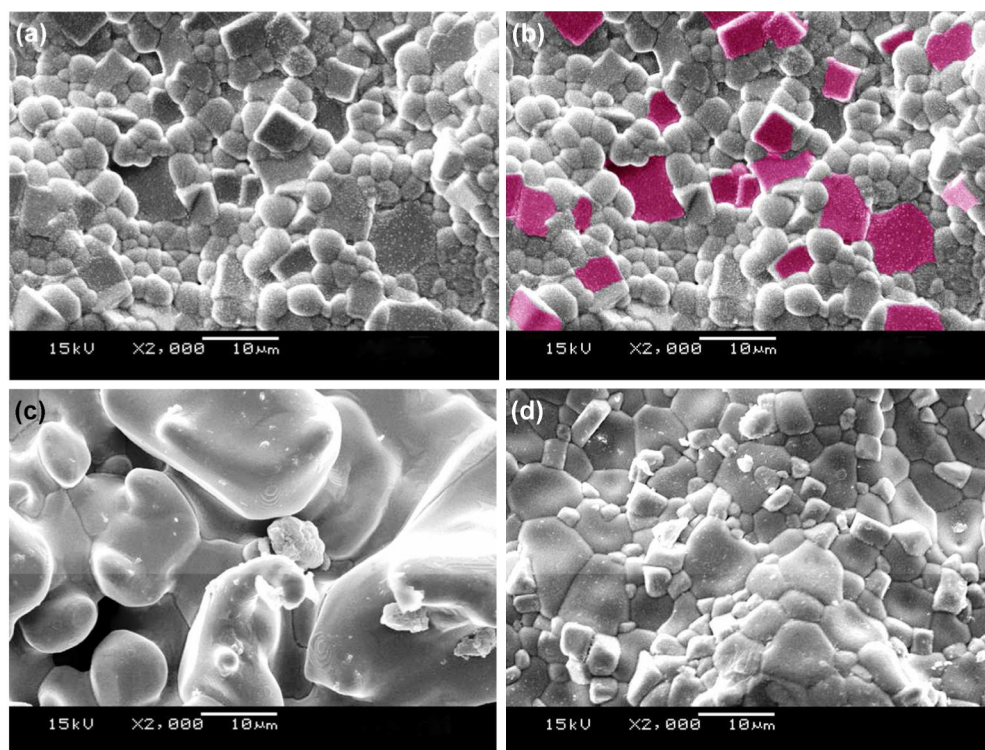
Figure 5. SEM micrographs of membranes sintered at 1400 °C for 4 h: (a) CGO−LBFZ40; (b) CGO−LBFZ40 (the magenta region represents clearly the perovskite crystal); (c) LBFZ; (d) YSZ−LBFZ40.
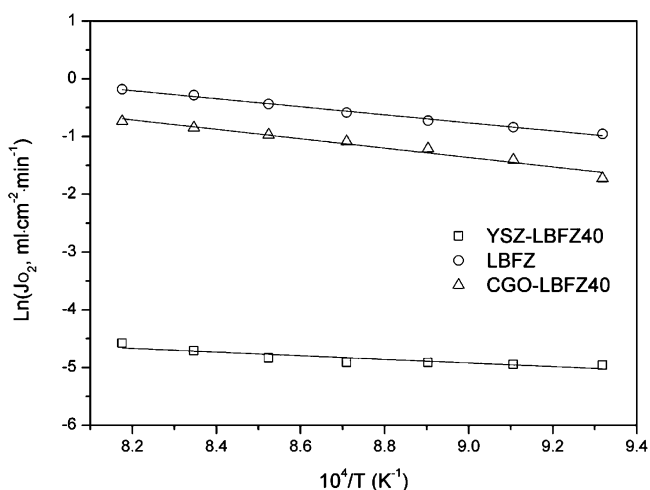

Figure 6. Oxygen permeation fluxes of LBFZ, YSZ−LBFZ40, and CGO−LBFZ40 membranes as a function of the temperature.

Figure 7. O_2-TPD profiles of the membrane samples LBFZ, YSZ−LBFZ40, and CGO−LBFZ40.

and LBFZ in the composite membrane. In light of the YSZ60−LBFZ40 membrane, it basically exhibited no oxygen permeation flux over the temperature range of study, which can be attributed primarily to degradation of LBFZ and disruption of this phase in the Ba-YSZ matrix.

A further examination on oxygen desorption of the material at different temperatures was conducted (O_2-TPD; Figure 7). The amount of oxygen desorbed from per unit mass of the LBFZ, CGO−LBFZ40, and YSZ−LBFZ40 specimens follows a decreasing order. Both LBFZ and CGO−LBFZ40 show a main O_2-TPD peak at 450 °C and a shoulder peak reaching a maximum at 650 °C. This corresponds to desorption of surface oxygen species and lattice oxygen species, respectively.[31,32] Relative to the pristine LBFZ membrane, the CGO−LBFZ40
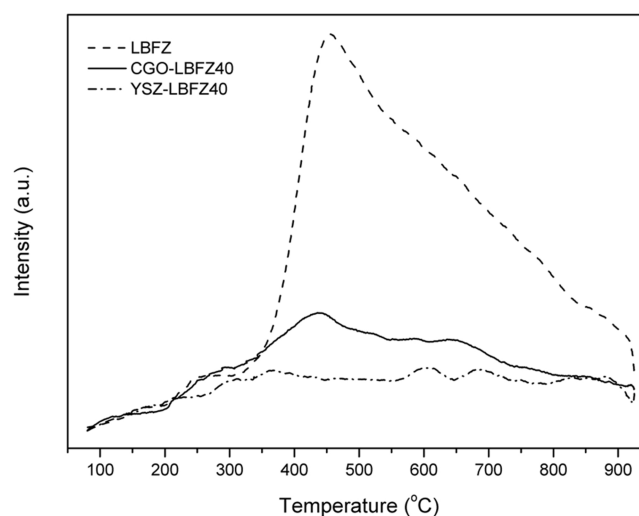
composite presents a far weaker O_2-TPD peak. By referring to their microstructures in Figure 5, the amount of oxygen adsorbed on LBFZ must be proportional to the exposed surface area. Therefore, the different O_2-TPD profiles can be attributed to the same reasoning as those responsible to the discrepancy in the TPR profiles of these two membranes. As for the YSZ−LBFZ40 composite membrane, unlike the above two membranes, this revealed negligible oxygen adsorption capability due to degradation of the LBFZ phase in the composite, as validated above.

Regarding the pristine LBFZ membrane, despite possessing a higher oxygen flux than the CGO−LBFZ membranes, its vulnerability inflates with an increase in the oxygen flux.

Annular cracks were inevitable in the tubular LBFZ membrane, particularly when the membrane was cooled. According to stoichiometry of LBFZ, 9% of its lattice oxygen sites are vacant. This structural character is vulnerable to lattice stress because of the increasing concentration gradient of the lattice oxygen vacancy between the two sides of the membrane. Electrochemical concentration polarization[33] leads to an accumulation of oxygen vacancies near the permeate side with continuing permeation of oxygen, which worsens until cracks occur as a result of the structural mismatch through the membrane. Contrary to the pristine LBFZ membrane matrix (Figure 5c), the structural continuity of the LBFZ phase is interrupted through the its mixing with the CGO phase in the composite membrane matrix, as identified in Figures 5a,b. The boundary generated between CGO and LBFZ gains thus could prevent the collection of oxygen vacancies over the length required to induce lattice stress in the LBFZ phase because the oxygen conductive CGO phase is mechanically stronger than the LBFZ phase. Indeed, the heterogeneous membrane matrix demonstrates an ability to overcome structural failure of the membrane throughout long and repetitive usage.

3.3. Oxygen Permeability of the Various CGO−LBFZ Composite Membranes.

In the dual-phase CGO−LBFZ composite membrane, an increase in the loading of the perovskite phase was initially expected to enhance the oxygen flux. However, the oxygen permeation experiment did not support such a trend with an increase in the LBFZ loading. Instead, an optimal combination was identified to achieve the highest oxygen flux (Figure 8). According to XRD character-
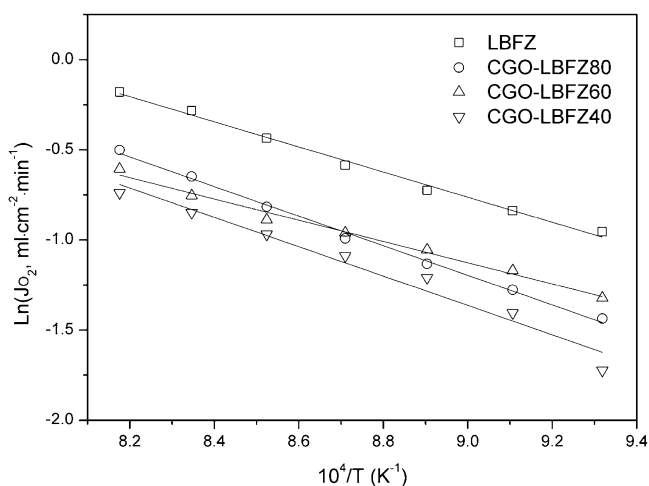
Figure 9. XRD patterns of the three CGO-LBFZ composites before and after TPR scan (denoted by R), where (∗) represents $BaCeO_3$ or $Ba(Ce_{0.9}Gd_{0.1})O_{2.95}$.

higher temperature range. This alternating of the flux values can be attributed to the temperature-driven crossing over the interfacial layer. With the exception of the temperature effect, the oxygen permeation through the composite membranes exhibits an increasing trend with increasing oxygen partial pressure gradient across the membrane (Figure 10). Similar to

Figure 8. Temperature-dependent oxygen permeation through the CGO−LBFZ composite membranes with 40 mL/min of helium as the sweep gas.

izization in Figure 9, a higher loading of LBFZ in the composite membrane causes a greater extent of diffusion of Ba^{2+} toward CGO. Hence, the impact of increasing LBFZ loading on oxygen transfer is balanced by the growth of the interfacial barrier layer consisting of the Ba-doped CGO and the degraded LBFZ phases. As a result, although the CGO−LBFZ40 membrane presented the lowest oxygen flux amid the three membranes over the entire temperature range under investigation, the CGO−LBFZ60 membrane performed better than the CGO−LBFZ80 membrane in the low-temperature range ($>10^4/T = 8.7$ K^{-1}). The CGO20−LBFZ80 membrane with the highest LBFZ loading could achieve higher oxygen flux only in the
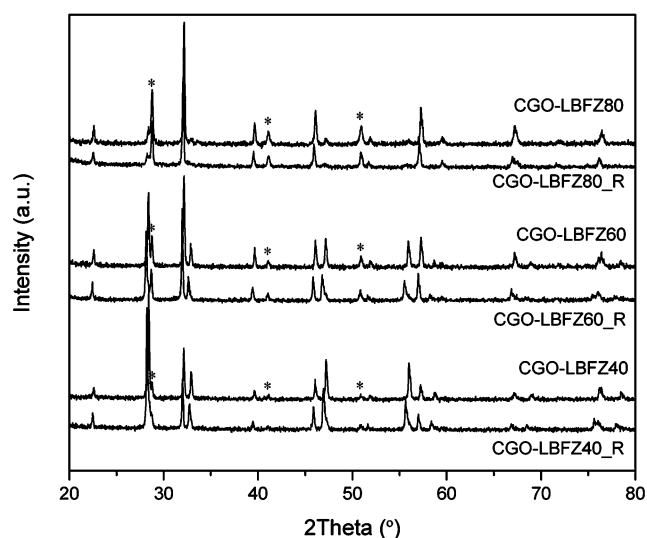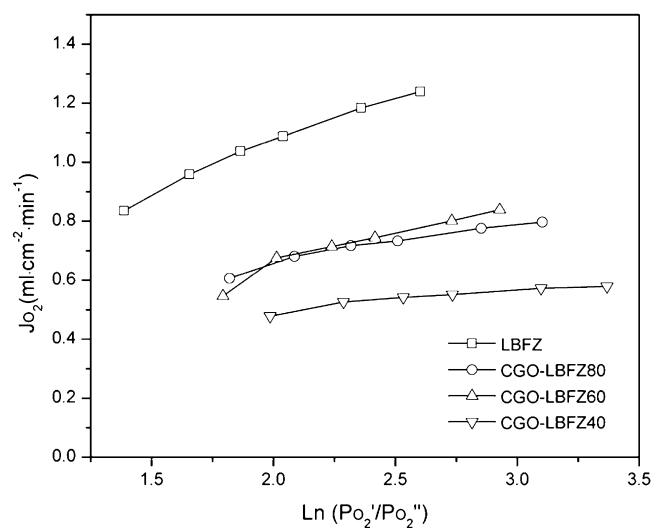
Figure 10. Oxygen permeation flux through a tubular CGO−LBFZ composite membrane at 950 °C under different oxygen partial pressure gradients.

the trend concluded from Figure 8, the trade-off gives rise to a maximum oxygen flux given by the CGO−LBFZ60 membrane in the range of the oxygen pressure gradient $[\ln(P_{O_2}'/P_{O_2}'') > 2.3]$. This composition gives the highest flux, 0.84 $cm^3/cm^2\cdot$ min, amid the composite membranes under the conditions of 950 °C and $\ln(P_{O_2}'/P_{O_2}'') = 2.8$. This optimizing outcome also confirms the involvement of the CGO phase in oxygen (O^{2-}) transfer as established earlier. Moreover, the favorable effect of LBFZ loading will be overtaken by the blocking effect of the interfacial layer at a higher oxygen pressure drop.

The O₂-TPD measurement of these three composite membranes also revealed discrepant behaviors affected by loading of the LBFZ phase (Figure 11). The figure shows that
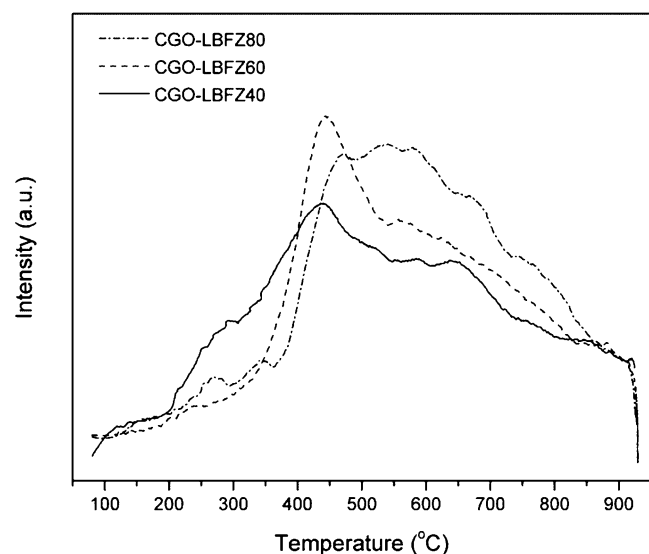

Figure 11. O₂-TPD profiles of CGO−LBFZ samples sintered at 1400 °C for 4 h.

the CGO−LBFZ60 composite exhibits a stronger desorption peak than the other two at around 450 °C, the characteristic desorption temperature of this type of surface site as defined before. It is presumed that degradation of LBFZ, caused by the retreatment of Ba²⁺ ions from it, also reduces the surface oxygen adsorption capability. Hence, the need for both a higher LBFZ loading and a lower extent in interfacial diffusion reaches an optimization state in the CGO−LBFZ60 composite. Furthermore, the LBFZ loading determines the magnitude of oxygen desorption from the lattice site occurring at higher temperatures; e.g., the CGO−LBFZ80 composite displays an expanded and stronger oxygen desorption peak. It is apparent that the surface of the LBFZ component is also vital to O²⁻ transfer in the bulk, as is also reflected by the oxygen permeation flux.

To further elucidate the experimental data of Figure 10, calculated oxygen permeation fluxes (Table 1) were generated using the method proposed by Zhu and Yang.[15] For example, specifications of the three membranes including the volume fraction, ionic conductivity of the two phases, and geometry of the membrane at the lowest pressure gradient (P_{O_2}'/P_{O_2}'') were taken into the consideration. The deviation of $J_{O_2,exp}/J_{O_2,cal}$ from unity states departure from the ideal model primarily because of the interfacial barrier layer and defects. Of the three deviations, the one exhibited by the CGO−LBFZ80 membrane reflects the most significant interfacial blockage to O²⁻ transfer.

On the contrary, the smallest deviation is demonstrated by the CGO−LBFZ60 membrane, which implies the least significant resistance to O²⁻ transport, and this perspective has been validated by the XRD and O₂-TPD studies, as described above.

The reducibility of the LBFZ phase change with its loading in the CGO−LBFZ composite has been investigated. Following elaboration in Figure 4, TPR profiles of the two composites except CGO−LBFZ40 display similar three-stage reduction profiles (Figure 12). The first reduction peak with similar
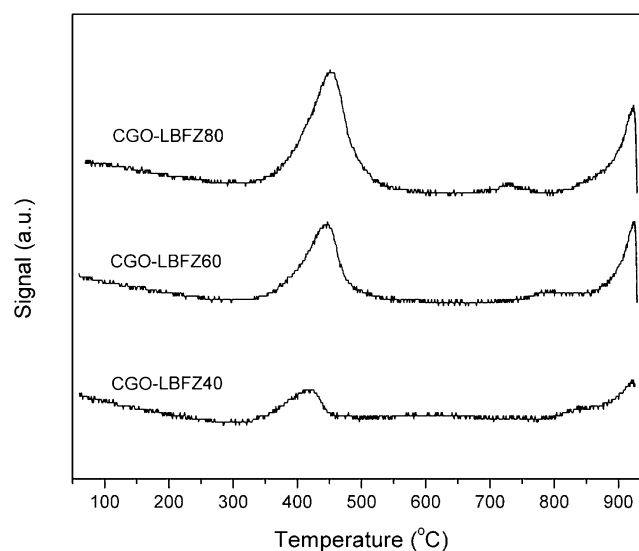

Figure 12. TPR profiles of CGO−LBFZ40, CGO−LBFZ60, and CGO−LBFZ80.

temperatures experiences intensity reduction with a decrease in the LBFZ loading. Regarding the second reduction peak, it shifts to higher temperature with an increase in the CGO loading, as observed in Figure 4. This confirms the stabilization role of the CGO phase, as proposed above. We further looked at the XRD spectra of these three composites samples after TPR scan (Figure 9) and found that the perovskite pattern still remains, albeit with a slight shift (<0.5°) in a lower 2θ direction. This verifies reduction of a small fraction of Fe⁴⁺/Fe³⁺ ions in LBFZ, which hence results in a minor lattice expansion. Besides expansion of the LBFZ phase, the CGO phase in the three samples also reveals a slightly larger d spacing caused by reduction of a trace amount of Ce⁴⁺ to Ce³⁺ despite not being reflected by the TPR measurement. Normally, the CGO phase exhibits both surface and bulk reduction peaks;[34] however, for the Ba²⁺-doped CGO, the interfacial diffusion layer on the CGO phase could play a suppression role in this reduction. Such a phenomenon can be regarded as a favorable factor to the composite membrane because increasing oxygen

Table 1. Experimental and Calculated Oxygen Permeation Fluxes ($J_{O_2,cal}$) through the CGO−LBFZ Membranes Swept by Helium (40 mL/min) at 950 °C^a

dual-phase composite	thickness (mm)	$\ln(P_{O_2}'/P_{O_2}'')$	$J_{O_2,exp}$ (cm³/cm²·min)	$J_{O_2,cal}$ (cm³/cm²·min)	$J_{O_2,exp}/J_{O_2,cal}$
CGO−LBFZ80	0.9	1.820	0.606	1.052	0.576
CGO−LBFZ60	1.0	1.790	0.546	0.778	0.702
CGO−LBFZ40	0.9	1.986	0.478	0.754	0.634

$^a P_{O_2}'/P_{O_2}''$: ratio of oxygen partial pressures at the air side to those at the permeate side.

vacancy concentration in pure CGO would often weaken its mechanical strength.

4. CONCLUSIONS

To resolve the fragile mechanical property of perovskite LBFZ under the oxygen permeation condition, fluorite CGO is identified to be an appropriate oxide electrolyte for compositing with LBFZ. A minor extent of interfacial reaction due to diffusion of Ba^{2+} ions from LBFZ to CGO occurs during the sintering process. The existence of a trivial interfacial phase ($BaCeO_3$) is favorable for promoting the structural intimacy between LBFZ and CGO as well as the chemical stability of LBFZ. This remark is based on characterizations of the XRD pattern and H_2-TPR and O_2-TPD. Contrary to CGO, fluorite YSZ is inappropriate to combine with LBFZ because of a severe extent of diffusion of Ba^{2+} ions into the YSZ phase, leading to degradation of the LBFZ phase. On the basis of this finding, the dual-phase CGO-LBFZx (x = 40, 60, and 80% by weight) composite membranes in a tubular shape were fabricated. Their oxygen permeability driven by helium purging on the permeate side was evaluated at various temperatures (800–950 °C) and partial pressure gradients of oxygen across the membrane $[\ln(P_{O_2}'/P_{O_2}'') = 1.73–3.38]$. The LBFZ phase composited with CGO displayed higher oxygen permeation than the pristine LBFZ membrane on the equal volume basis. This suggests participation of the CGO phase in mass transportation of the O^{2-} ion. The CGO–LBFZ60 membrane was deemed to offer the best oxygen permeation flux in either the lower temperature range or the higher partial pressure gradient range amid the three membranes; for example, it provided 0.84 $cm^3/cm^2 \cdot min$ at 950 °C and $\ln(P_{O_2}'/P_{O_2}'') = 2.8$. Finally, the CGO–LBFZ membranes completely rectify the structure vulnerability associated with the pristine LBFZ membrane.

■ AUTHOR INFORMATION

Corresponding Author
*E-mail: chehongl@nus.edu.sg. Tel: +65-6516 502. Fax: +65-6779 1936.

Author Contributions
The manuscript was written through the contributions of all authors. All authors have given approval to the final version of the manuscript. These authors contributed equally to the manuscript.

Notes
The authors declare no competing financial interest.

■ REFERENCES

(1) Sunarso, J.; Baumann, S.; Serra, J. M.; Meulenberg, W. A.; Liu, S.; Lin, Y. S.; Diniz da Costa, J. C. *J. Membr. Sci.* **2008**, *320* (1–2), 13–41.
(2) Kilner, J. A.; De Souza, R. A.; Fullarton, I. C. *Solid State Ionics* **1996**, *86–88* (2), 703–709.
(3) Stevenson, J.; Armstrong, T.; Carneim, R.; Pederson, L.; Weber, W. *J. Electrochem. Soc.* **1996**, *143* (9), 2722–2729.
(4) Ullmann, H.; Trofimenko, N.; Tietz, F.; Stöver, D.; Ahmad-Khanlou, A. *Solid State Ionics* **2000**, *138* (1–2), 79–90.
(5) Dusastre, V.; Kilner, J. A. *Solid State Ionics* **1999**, *126* (1–2), 163–174.
(6) Peng, Z.; Liu, M.; Balko, E. *Sens. Actuators, B* **2001**, *72* (1), 35–40.
(7) Nigge, U.; Wiemhöfer, H. D.; Römer, E. W. J.; Bouwmeester, H. J. M.; Schulte, T. R. *Solid State Ionics* **2002**, *146* (1–2), 163–174.
(8) Zeng, Y.; Lin, Y. S.; Swartz, S. L. *J. Membr. Sci.* **1998**, *150* (1), 87–98.
(9) Tan, X.; Liu, Y.; Li, K. *AIChE J.* **2005**, *51* (7), 1991–2000.
(10) Shao, Z.; Xiong, G.; Cong, Y.; Yang, W. *J. Membr. Sci.* **2000**, *164* (1–2), 167–176.
(11) Liu, S.; Tan, X.; Shao, Z.; Da Costa, J. C. D. *AIChE J.* **2006**, *52* (10), 3452–3461.
(12) Balachandran, U.; Ma, B.; Maiya, P. S.; Mieville, R. L.; Dusek, J. T.; Picciolo, J. J.; Guan, J.; Dorris, S. E.; Liu, M. *Solid State Ionics* **1998**, *108* (1–4), 363–370.
(13) Ito, W.; Nagai, T.; Sakon, T. *Solid State Ionics* **2007**, *178* (11–12), 809–816.
(14) McGrath, K. M. *Adv. Mater.* **2001**, *13* (12–13), 993–996.
(15) Zhu, X.; Yang, W. *AIChE J.* **2008**, *54* (3), 665–672.
(16) Pei, S.; Kleefisch, M. S.; Kobylinski, T. P.; Faber, J.; Udovich, C. A.; Zhang-McCoy, V.; Dabrowski, B.; Balachandran, U.; Mieville, R. L.; Poeppel, R. B. *Catal. Lett.* **1995**, *30* (1–4), 201–212.
(17) Huang, B. X.; Malzbender, J.; Steinbrech, R. W.; Singheiser, L. *Solid State Ionics* **2009**, *180* (2–3), 241–245.
(18) Juste, E.; Julian, A.; Etchegoyen, G.; Geffroy, P. M.; Chartier, T.; Richet, N.; Del Gallo, P. *J. Membr. Sci.* **2008**, *319* (1–2), 185–191.
(19) Kharton, V. V.; Yaremchenko, A. A.; Patrakeev, M. V.; Naumovich, E. N.; Marques, F. M. B. *J. Eur. Ceram. Soc.* **2003**, *23* (9), 1417–1426.
(20) Efimov, K.; Halfer, T.; Kuhn, A.; Heitjans, P.; Caro, J.; Feldhoff, A. *Chem. Mater.* **2010**, *22* (4), 1540–1544.
(21) Li, Q. M.; Zhu, X. F.; He, Y. F.; Yang, W. S. *Sep. Purif. Technol.* **2010**, *73* (1), 38–43.
(22) Kim, J.; Lin, Y. S. *J. Membr. Sci.* **2000**, *167* (1), 123–133.
(23) Kharton, V. V.; Kovalevsky, A. V.; Viskup, A. P.; Figueiredo, F. M.; Yaremchenko, A. A.; Naumovich, E. N.; Marques, F. M. B. *J. Electrochem. Soc.* **2000**, *147* (7), 2814–2821.
(24) Kharton, V. V.; Marques, F. M. B. *Curr. Opin. Solid State Mater. Sci.* **2002**, *6* (3), 261–269.
(25) Kharton, V. V.; Kovalevsky, A. V.; Viskup, A. P.; Shaula, A. L.; Figueiredo, F. M.; Naumovich, E. N.; Marques, F. M. B. *Solid State Ionics* **2003**, *160* (3–4), 247–258.
(26) Zhu, X. F.; Li, M. R.; Liu, H. Y.; Zhang, T. Y.; Cong, Y.; Yang, W. S. *J. Membr. Sci.* **2012**, *394*, 120–130.
(27) Luo, H. X.; Jiang, H. Q.; Klande, T.; Cao, Z. W.; Liang, F. Y.; Wang, H. H.; Caro, J. *Chem. Mater.* **2012**, *24* (11), 2148–2154.
(28) Gong, Z.; Yin, X.; Hong, L. *J. Electrochem. Soc.* **2010**, *157* (8), E129–E134.
(29) Yin, X.; Hong, L.; Liu, Z. L. *J. Membr. Sci.* **2006**, *268* (1), 2–12.
(30) Peña, M. A.; Fierro, J. L. G. *Chem. Rev.* **2001**, *101* (7), 1981–2017.
(31) Barbero, B. P.; Gamboa, J. A.; Cadús, L. E. *Appl. Catal., B* **2006**, *65* (1–2), 21–30.
(32) Ferri, D.; Forni, L. *Appl. Catal., B* **1998**, *16* (2), 119–126.
(33) Sammells, A. F.; Mundschau, M. V. *Nonporous Inorganic Membranes: For Chemical Processing*; Wiley-VCH: Weinheim, Germany, 2006; p 187.
(34) Katta, L.; Sudarsanam, P.; Thrimurthulu, G.; Reddy, B. M. *Appl. Catal., B* **2010**, *101* (1–2), 101–108.